Shear-flow-based chromatographic separations as an alternative to pressure-driven liquid chromatography

G. Desmet*, N. Vervoort, D. Clicq, A. Huau, P. Gzil, G.V. Baron

Vrije Universiteit Brussel, Department of Chemical Engineering, Pleinlaan 2, 1050 Brussels, Belgium

Abstract

It is only by developing specially designed injection and detection systems that shear-driven chromatography can become a viable alternative to HPLC. In the present paper, a dedicated zero dead-volume injection procedure is presented with which sample volumes can be injected reproducibly in the required picoliter range. In addition, a transversal detection groove system is designed which should allow to perform on-line UV–VIS absorption measurements with path lengths in the millimeter range, with an acceptable theoretical plate loss (only 20% in a 5 cm long channel) and acting as a nearly perfect wave guide. © 2002 Elsevier Science B.V. All rights reserved.

Keywords: Shear-driven chromatography; Injection methods; Detection, LC; Computational fluid dynamics; Instrumentation

1. Introduction

1.1. General

The present paper mainly focuses on the injection and detection aspects of ultra-miniaturised chromatographic systems (i.e., systems with a sub-μm channel thickness). The use of such ultra-miniaturised systems appears very attractive from the point of view of the increased separation kinetics and resolution, but injection and detection can be expected to be very critical aspects: the ability to inject and detect minute sample amounts is namely generally recognized [1–5] as the main bottleneck for miniaturised chromatographic systems such as on-chip CE and capillary electrochromatography (CEC). For on-chip LC or HPLC [6,7], an additional bottleneck is found in the connection and mechanical fracture problems brought about by the large required inlet pressures.

Recently [8], we have proposed the concept of shear-driven chromatography (SDC) as a simple means to circumvent the inlet pressure limitation. The concept is based on the use of channels whose wall is axially split into two independent parts, one part being substantially longer than the other part. By sliding the longer part past the shorter part, fluids can be dragged through the channel opening formed by the two parts without the need for a raised inlet pressure. The established flow displays a linear velocity profile (except for a small region of width $\sim d$ near the side-walls) and therefore has a mean axial velocity approximately equal to one half of the moving wall velocity:

$$u = u_{\text{wall}}/2 \tag{1}$$

independently of the channel thickness or length and independent of the nature (viscosity, conductivity, pH, ...). Accounting the linear velocity profile, it

*Corresponding author. Tel.: +32-2-629-3251; fax: +32-2-629-3248.

E-mail address: gedesmet@vub.ac.be (G. Desmet).

can be shown that the theoretical plate height in a shear-driven flow channel is given by [8]:

$$H = 2 \cdot \frac{D_m}{u} + \frac{2}{30} \cdot \frac{1 + 7k + 16k^2}{(1 + k)^2} \cdot u \cdot \frac{d^2}{D_m} + \frac{2}{3}$$

$$\cdot \frac{k}{(1 + k)^2} \cdot u \cdot \frac{d_f^2}{D_s} \qquad (2)$$

As the inlet pressure limitation is omitted, the concept is ideally suited to further down-scale LC systems towards the sub-μm channel thickness range. Fig. 1 clearly illustrates the advantage of a pressure drop-less operation: whereas in a pressure-driven system such as HPLC, a reduction of the characteristic diffusional distance from $d_p = 3$ μm to $d_p = 1$ μm is counter-productive [2] and leads to an increase of the analysis time for all separations with $N > 5000$, the effect of a similar miniaturisation of the SDC system is purely positive and leads to a strong decrease of the required analysis time.

An experimental proof for the SDC concept has very recently [9] been obtained in 4 μm channels carrying a mobile phase liquid flow past a 4 μm thick layer of commercial RP-HPLC particles immobilized within a porous polyacrylic matrix. A recent example of the separations which can be performed with the given system is shown in Fig. 2. The technical details of the experiments are given in [9], and current work is underway to further

downscale the system. This is required, because, as can be noted from Fig. 1, the 4 μm channel system is still too large to surpass the separation speed and resolution of HPLC. It can also be seen from Fig. 1 that, in order to make a significant leap, the sub-μm range has to be entered. Shear-driven flows through sub-μm channels can be established relatively easily [10]: even down to the 100 nm range no significant deviation from the expected theory was observed. However, just as for any other miniaturised technique, injection and detection become very critical issues.

1.2. Injection and detection requirements and proposed concepts

As the theoretical plate height H in a chromatographic system scales in a directly proportional way to the channel thickness or particle diameter, and as the peak width increase due to the chromatographic process also varies in a directly proportional way with H ($w_b = 4N^{1/2}H$), it is obvious that each attempt to increase the separation resolution of a given chromatographic system by miniaturizing the channel dimensions also inevitably brings about a reduction of the peak volumes [1]. Injection and detection hence are performance limiting issues in the further development of miniaturised chromatographic systems [1,11,12]. With the sub-μm channel systems needed to realize its full potential, this problem appears to be a fortiori true for SDC. However, as will be demonstrated further down below, the unusual design and operation mode of the shear-driven flow channels enables a number of injection and detection solutions with which the expected problems can be overcome.

To calculate the maximal allowable injection plug width in SDC for the most critical envisioned case (i.e., for 100 nm thick channels operated at $u = u_{opt}$, and hence yielding the largest envisioned separation resolutions), the following reasoning can be followed. Noting that from Eq. (2) the minimal theoretical plate height value ($u = u_{opt}$-conditions) can be calculated to be [10] given by:
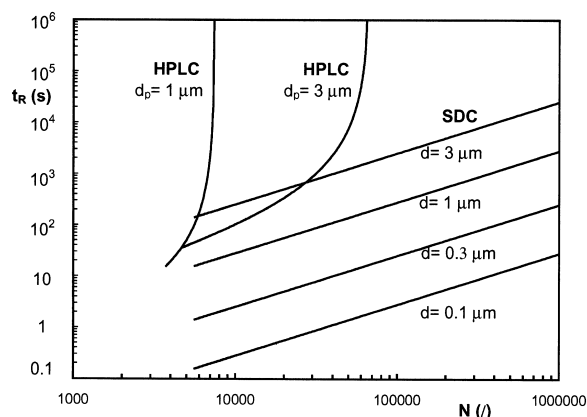

Fig. 1. Comparison of the required analysis time in HPLC and SDC as a function of the required theoretical plate number. All points along the presented curves correspond to a critical pair separation with $K = 3$ (graph taken from [9]).

$$H_{min} = 4 \cdot \frac{d}{(1 + k)} \cdot \sqrt{\frac{1 + 7k + 16k^2}{30} + \frac{k}{3} \cdot \frac{(d_f/d)^2}{(D_s/D_m)}}$$
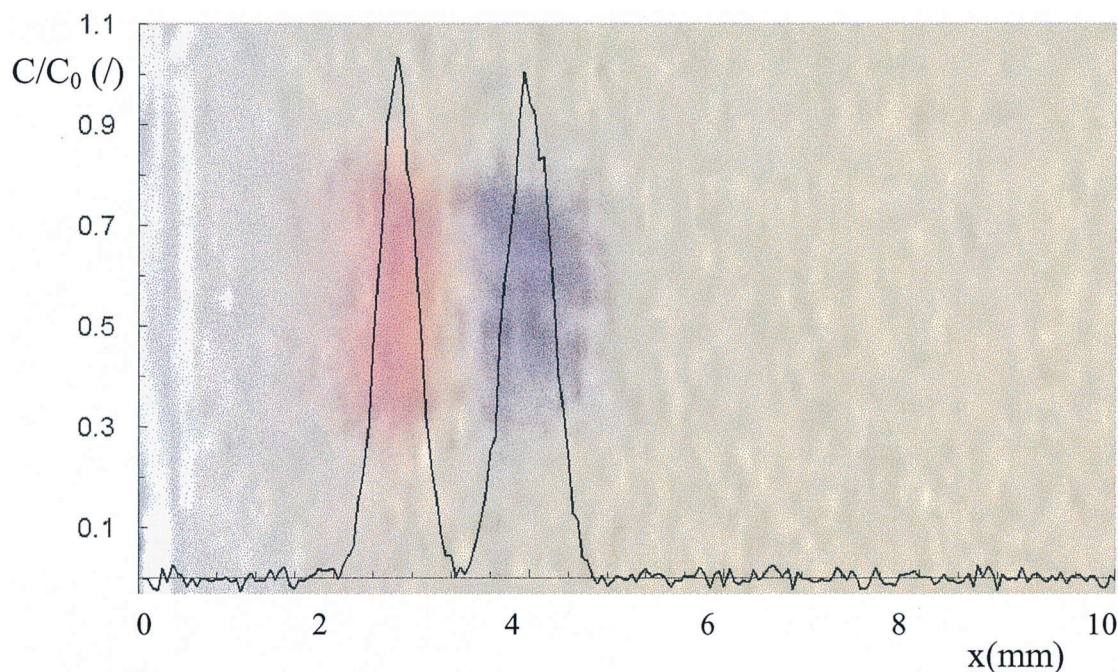
$$(3)$$

Fig. 2. Photographic image (taken at $t = 6$ s) and overlaid colour intensity scan of a chromatographic separation of a (50 mM/50 mM) Rhodamine B/methylene blue in a planar shear-driven channel system (channel thickness$=4$ μm) using water–methanol (30:70) mobile phase.

and further assuming a rectangular shape for the injected sample bands such that:

$$\sigma_{inj}^2 = \frac{w_{b,inj}^2}{12} \qquad (4)$$

the relative loss in theoretical plate number due to the injection band width in the most critical case (i.e., for $H = H_{min}$) can be calculated to be:

$$\frac{N_{eff,inj}}{N_{theo}} = \frac{\sigma_{col}^2}{\sigma_{inj}^2 + \sigma_{col}^2} = \frac{H_{min}L}{\sigma_{inj}^2 + H_{min}L} \qquad (5)$$

With Eqs. (3)–(5), and considering a typical retention factor of $k = 3$ (leading to $u = u_{opt} = 1.7$ cm/s), a relation between the allowable plate loss and the corresponding injection band widths $w_{b,inj}$ can be established. The results are given in Table 1. It can clearly be noted that even the most stringent condition ($L = 1$ cm, and only 10% loss of theoretical plate number) still leads to an allowable injection band width of the order of $w_{b,inj} = 50$ μm, whereas in "longer" channels (order 3 to 5 cm) injection band widths of the order of 100 μm to 150 μm still allow the realization of up to 200 000 theoretical plates. In the present study a refined version (see Fig. 3) of the injection scheme already proposed in [9] has been used to investigate whether sample plugs in the order of 50 to 100 μm can be injected with a sufficient degree of reproducibility. Table 1 also gives the expected peak width $w_{b,det}$ at the detector, defined as:

$$w_{b,det} = 4\sqrt{\sigma_{inj}^2 + \sigma_{col}^2} \qquad (6)$$

These values will be used further down below for the design of a dedicated detection cell.

A number of ingenious detection schemes has already been proposed in the past to enhance the detection sensitivity of on-chip chromatographic systems [3,5,12]. The large available optical path length in the flat-rectangular SDC channels would in principle allow to benefit maximally from the Beer–Lambert law for UV–Vis absorption detection. The possibility to use UV–Vis absorption detection is also highly preferred because it is much more

Table 1
Maximally allowable injection peak widths $w_{b,inj}$ and corresponding detector peak widths $w_{b,det}$ calculated from Eqs. (3)–(6) for a 100 nm SDC channel operated at $u = u_{opt}$ with $k = 3$, and with $d_f = 10$ nm, $D_m = 10^{-9}$ m^2/s, $D_s = 5 \cdot 10^{-10}$ m^2/s ($\mu_{opt} = 1.7$ cm/s)

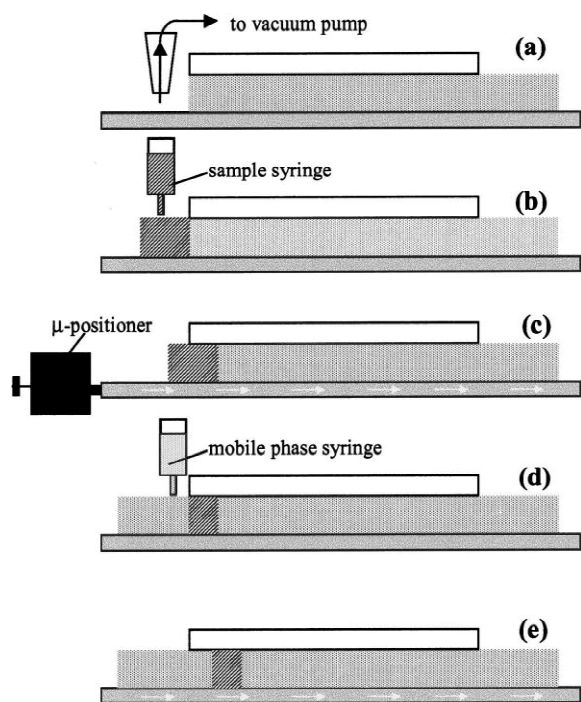| L (cm)	H_{min} (μm)	N_{theo}	Plate loss (%)	$w_{b,inj}$ (μm)	$N_{eff,inj}$	$w_{b,det}$ (μm)
1	0.18	51 411	20	73	41 129	189
1	0.18	51 411	10	49	46 270	178
2	0.18	107 125	20	104	85 700	267
2	0.18	107 125	10	69	96 412	252
3	0.18	162 960	20	127	130 368	328
3	0.18	162 960	10	85	146 664	309
5	0.18	274 710	20	164	219 768	423
5	0.18	274 710	10	109	247 239	399
10	0.18	554 176	20	232	443 341	598
10	0.18	554 176	10	154	498 759	564

Fig. 3. Schematic representation (longitudinal view, not to scale) of the injection procedure. First, an aspirating pump is used to remove the mobile phase fluid covering the movable wall plate in front of the channel inlet (a). Subsequently, a small amount of the sample liquid is put in front of the channel inlet with a conventional liquid syringe (b). Then, the movable wall plate is displaced over a predefined distance with the micro-manipulator in order to fill the channel inlet section with the tracer (c). Subsequently, the non-entered sample is flushed away (d) with pure mobile phase liquid, and the motion of the movable wall plate is resumed (e).

versatile than laser-induced fluorescence, which due to its independence of the optical path length, currently seems nearly the only viable detection resort for on-chip systems [13,14]. Considering the Beer–Lambert law for absorption detection:

$$\mathrm{Log}(I/I_0) \sim C_{max} \lambda_w \tag{7}$$

and noting that SDC channels can typically be made several 100 μm or even millimeters wide [8,10], this implies that, if it could be possible to guide a light beam transversally through the channel cross-section, sub-μm SDC would yield the same detection sensitivity as the macro-scale HPLC systems (the outlet peak concentration C_{max} only depends on the number of theoretical plates, and can hence be taken identical for HPLC and SDC). The problem with sub-μm SDC however is that the channel thickness is too thin to allow the non-dissipating passage of a light beam: a gap of at least two times the light wavelength is needed.

This has lead us to the introduction of a transversal detection groove system, with a lay-out and dimensions (2 μm deep and 2 μm axial width) as depicted in Fig. 4. The proposed concept obviously has the potential to combine the extremely powerful separation resolutions achievable in a 0.1 μm thick channel with the detection sensitivities corresponding to an optical path length of several millimeter. The proposed concept furthermore also has an important advantage in that the light is nearly completely prevented from straying in the axial direction (channel thickness d has sub-wavelength dimensions). This advantage is an exclusive feature reserved to separation channels which are significantly thinner
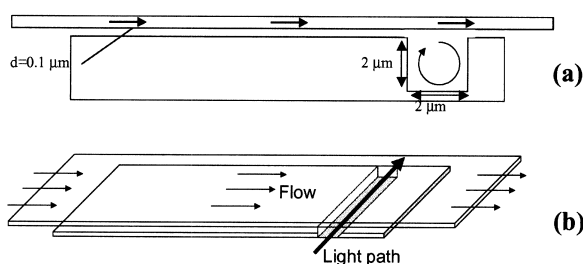
Fig. 4. Two dimensional (a) and three dimensional (b) view of novel transversal detection groove system for UV–Vis absorption detection in sub-μm SDC channels.

than the wavelength of the incident light, as is the case for the presently considered ultra-thin SDC channels.

The above advantages can however only be realized when the separation resolution achieved in the separation channel is not too strongly deteriorated by the mixing and dispersion effects introduced by the presence of the detection groove. To ascertain that this is not the case, a first argument can be found by comparing the expected detector peak volume and the detection groove volume. Considering that the expected peak widths in sub-μm SDC will typically still be larger than 200 μm (cf. final column in Table 1), it can be derived that the peak volume in shear-driven SDC in a $d = 0.1$ μm channel is proportional to $200 \times 0.1 = 20$ μm^2, whereas the volume of the detection cell is proportional to $2 \times 2 = 4$ μm^2. This implies that the volume of the detector cell is about 5

times smaller than the peak volume, such that it can be anticipated that the detection groove will indeed not cause too much peak broadening. In the present study, a second, and more conclusive argument will be obtained from computational fluid dynamics (CFD) simulations of the flow of chromatographic peaks through the detection groove. In the recent years, CFD has becomes an increasingly important tool in the design of miniaturized chromatographic systems [15,16]. Because of the accuracy with which the flow field can be calculated under laminar conditions, CFD results for laminar flows are, provided that the computational grid is sufficiently refined, perfectly reliable [17].

2. Experimental

2.1. Injection experiments in 0.1 and 0.4 μm thin channels

The operating principle of the shear-driven channel system in our experimental set-up is similar to that used in previously reported studies [9,10]. In the present study, a specially designed metal holding piece (Fig. 5) is used to connect the stationary channel wall plate to the lens ($4 \times$ magnification) of an optical microscope (Microphot-FXA, Nikon), allowing to both accurately control and monitor the displacement of the movable channel wall plate.
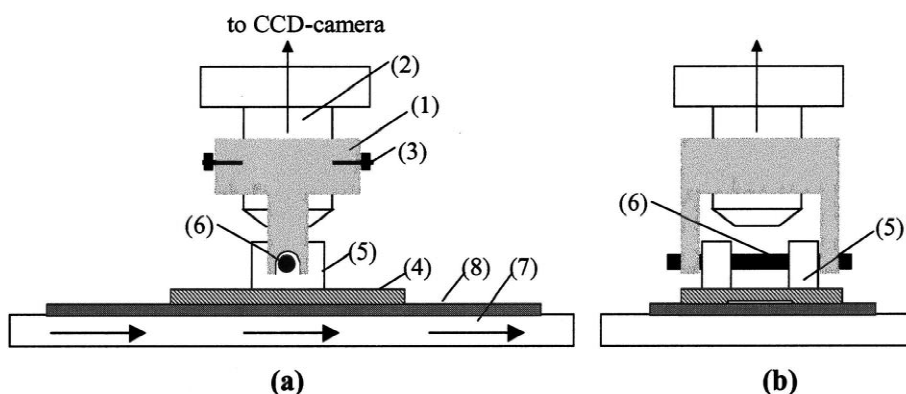

Fig. 5. Sketched side-view (a) and front view (b) of experimental microscope set-up, showing the metal holding piece (1), attached to the microscope lens (2) by means of the fixation bolts (3). The stationary channel plate (4) carries two plastic blocks (5). The stationary channel plate is held in place by a metal rod (6) running through the plastic blocks and the holder piece. The optical table (7) is used to support and translate the movable channel plate (8).

Highly polished fused-silica substrates (with flatness $\lambda/10$) were used for both the movable and the stationary wall plate. The substrate for the movable plate had circular dimensions (diameter 50 mm), whereas the stationary platelet had rectangular dimensions (20×15 mm), and carried a half open channel obtained by HF wet etching. In all the experiments, the channels were 5 mm wide, with the flow running across the shortest dimension of the stationary platelet. Etch depths were controlled [10] with a Talystep depth profile meter (Rank Taylor Hobson, UK). Two different channel depths were considered (0.1 and 0.4 μm). The working fluid was deionized Milli-Q water, and a highly concentrated Rhodamine B solution (0.1 M) was used as the tracer liquid. The flow was monitored with a non-cooled CCD camera (DCX-107P, Sony, Belgium) and the video images were captured with a DC10 video capture card (Pinnacle Systems, Germany). At regular intervals, still images were taken and colour intensity plots were made with a commercial photo-editing package (MS Photo Editor), using a self-written Mathlab routine to automate the process. The diffusion coefficient of the Rhodamin B tracer was determined from a series of independent experiments (cf. Section 3.1), by applying a step gradient of highly concentrated tracer at the channel inlet and by recording the penetrating tracer concentration profiles. The diffusion coefficient D_m was then determined from the relation between the increasing concentration profile variance σ_x^2 and the time. The theoretical relation between the σ_x^2 values of the penetrating tracer front (cf. experimentally observed tracer diffusion curves presented in Fig. 6a) and the diffusion time was determined from the solution of the unsteady tracer diffusion equation [18,19]:

$$\frac{\partial C}{\partial t} = D_m \cdot \frac{\partial^2 C}{\partial x^2} \tag{8a}$$

with the appropriate initial and boundary conditions:

$C = C_0$ at $x = 0$ (for all $t \geq 0$)   and:

$C = 0$ at $x = +\infty$ (for all $t \geq 0$) \hfill (8b)

This yielded [18]:

$$\sigma_{x,\text{diff}}^2 = 0.551 D_m t \tag{9}$$
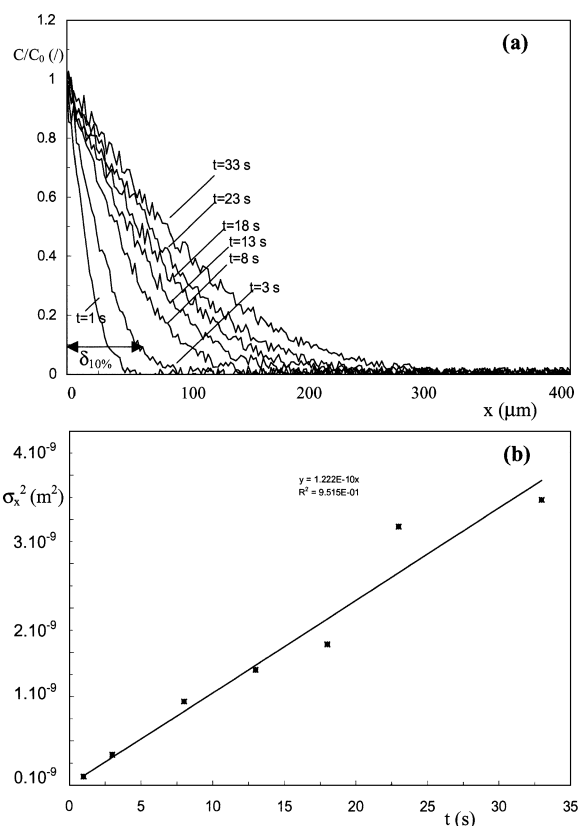
and:

Fig. 6. Colour intensity scans of a tracer band diffusing into the channel (a) and corresponding plot of σ_x^2 versus time (b) used for the determination of D_m according to Eq. (9).

$$\delta_{10\%}^2 = 5.382 D_m t \tag{10}$$

wherein $\delta_{10\%}$ is the distance over which the tracer curve has penetrated into the channel at a concentration value of 10% of its maximum (see Fig. 6). Calculating the surface under the penetrating tracer concentration curves (yielding the 0th order moment M_0 of the tracer distribution) according to:

$$M_0 = \int_{-\infty}^{+\infty} C/C_0 \cdot dx \tag{11}$$

this value has been used to calculate the tracer peak volume via:

$$V_p = M_0 d\lambda_w \tag{12}$$

Numerically solving Eq. (8) with the given bound-

ary and initial conditions yielded the following relation between M_0 and t:

$$M_0 = 1.296 D_m t \tag{13}$$

Eqs. (10)–(13) allow to estimate the (undesired) amount of sample diffusing into the channel during the waiting times of the injection procedure (cf. Section 4.1).

The most important part in the injection set-up was a manually operated micro-manipulator (460P-X, Newport, Belgium), positioned as shown in Fig. 3, and driving the displacement of the optical microscope Table during the injection with an overall displacement control of the order of 5 μm. Prior to the tracer injections, the mobile phase fluid covering the movable wall plate in front of the channel inlet is aspirated away using a micro-pipette tip connected to a vacuum pump with a flexible tube (cf. Fig. 3a). As no separate injection channels are involved, the technique can be considered to be a truly zero dead-volume technique.

2.2. Flow simulations

The flow through the transversal detection groove system depicted in Fig. 4 was calculated using the two-dimensional double precision solver of a commercial Computational Fluid Dynamics package (Fluent 5.0) run on a Compaq XP 1000 workstation. The pressure-velocity coupling was solved using the SIMPLE algorithm. The grid used to discretize the flow equations was generated with Gambit software run on the same workstation. Two cases were considered: a groove with rectangular walls (depth δ_G and axial width λ_G), and a groove with semi-circular walls (cf. Fig. 9). As the flow is fully laminar, the flow field can be calculated with a high degree of accuracy [17]. Validation checks were performed for flows through channels with simple geometry for which the flow field is exactly known from existing analytical expressions [20]. A better than 0.01% agreement with the theoretical mean flow velocities was obtained in all the cases. The peak dispersion was calculated using the mass balance solver of the same Fluent package. Again, the

validity of the simulated results was checked by comparing with known situations.

3. Results

3.1. Determination of the diffusion coefficient

Fig. 6a shows a typical plot of the observed penetrating tracer concentration profiles obtained after contacting the channel inlet with pure, undiluted tracer solution. From the concentration profiles, the second order spatial moment σ_x^2 was calculated and plotted versus the experimental time, yielding a straight line relationship as represented in Fig. 6b. The value of the diffusion coefficient can then directly be determined from the line slope, which, according to Eq. (9), is equal to $0.551 D_m$. The experiment was repeated five times yielding:

$$D_m = 2.2 \cdot 10^{-10}\,\mathrm{m^2/s}\,(\pm 0.4 \cdot 10^{-10}\,\mathrm{m^2/s}) \tag{14}$$

3.2. Injection experiments in 0.1 and 0.4 μm channels

A large number of injection experiments was performed in both the 0.1 and 0.4 μm channels. Apart from the magnitude of the recorded tracer intensity, no effect of the channel thickness on the injected concentration profile could be observed. Two typical examples of the shape of the obtained injection bands are shown in Fig. 7. The profile (obtained after an injection procedure in which the movable wall was displaced over a given distance $w_{displ} = 150$ μm) does not correspond to the expected rectangular injection block shape with axial width = 75 μm (cf. Eq. (15)), although the shape of the expected rectangular block can still somewhat be discerned (cf. dashed lines in Fig. 7). The peaks are also clearly asymmetric, indicating that channel inward diffusion plays an important role in the injection process. This is due to the fact that, as all the steps in the injection procedure were carried out manually, the entire injection process usually took 3 to 5 s (cf. t_{inj} values in Table 2). As can be noted from Fig. 6a, diffusion penetration distances can be up to 50 to 100 μm during this time, and can hence
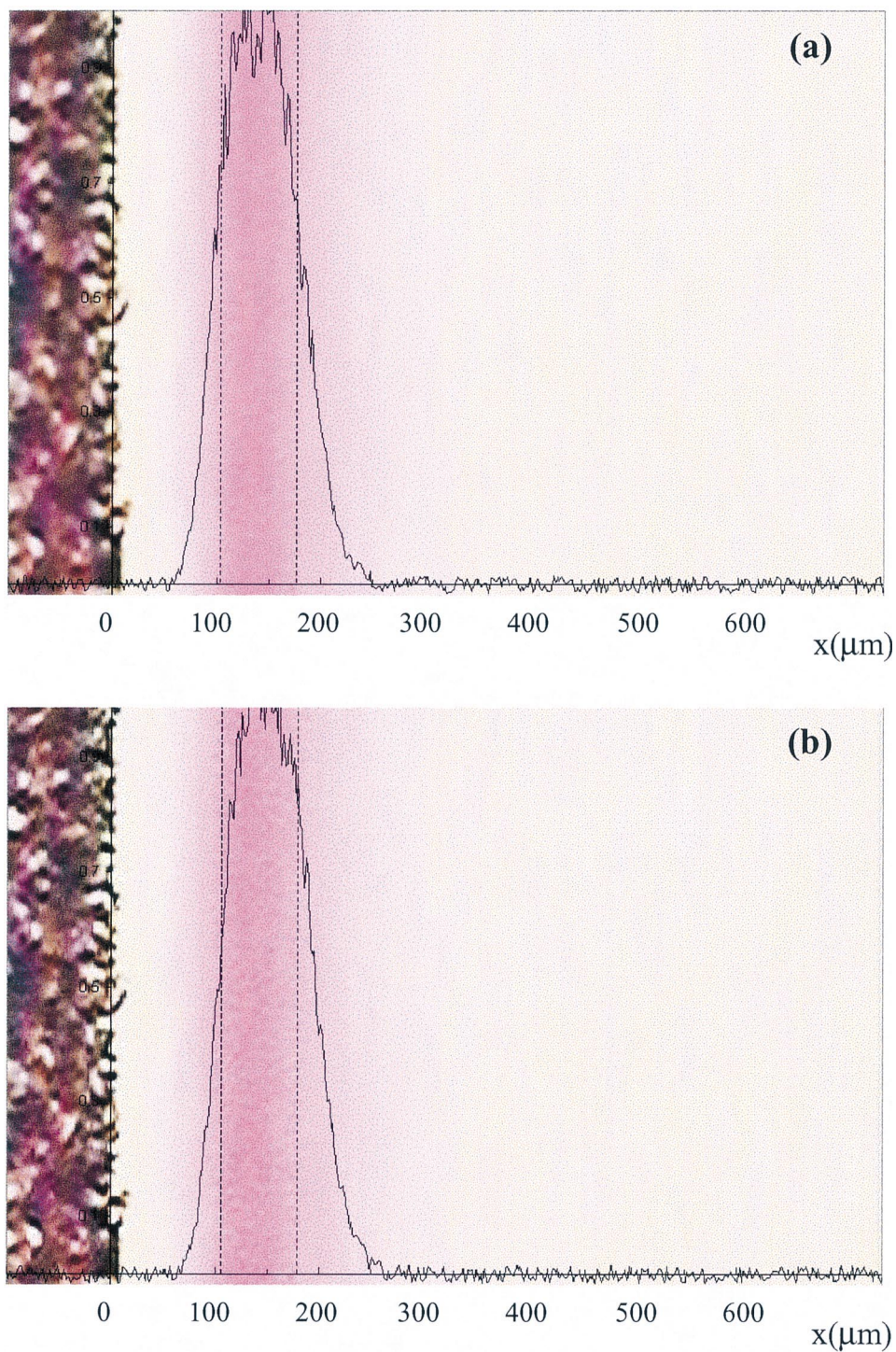
Fig. 7. Still images and colour intensity scans of two different tracer band injections (a and b) obtained by shifting the movable channel plate over a distance $w_{\text{displ}} = 150$ μm (displacement velocity $\cong 0.1$ mm/s, channel depth $= 0.1$ μm). Peak volumes were determined to be $V_p = 10.1$ pl for (a) and $V_p = 9.5$ pl for (b).

Table 2
Experimental injection peak widths $w_{b,inj}$ (taken at 10% of the concentration height, the calculated corresponding peak volumes V_p, and the peak width value $w_{inj,corr}$ obtained after correcting for the diffusion flux contribution to the injection process (duration t_{inj} of injection process was estimated from the video recordings)

w_{displ} (μm)	$w_{inj,conv}$ (μm)	$w_{b,\,inj}$ (μm)	V_p (pl)	t_{inj} (s)	$w_{inj,\,corr}$ (μm)
100	50	145	9.0	5	68
100	50	148	8.3	5	71
100	50	145	9.0	5	68
100	50	138	8.0	5	61
100	50	138	8.1	4	69
100	50	132	8.4	4	63
100	50	128	7.7	4	59
100	50	126	8.5	4	57
200	100	185	13.8	5	108
200	100	173	13.7	5	96
200	100	172	13.8	5	95
200	100	184	14.0	5	107
200	100	179	13.2	4	110
200	100	159	13.6	4	90
200	100	170	12.9	3	110
200	100	155	13.0	3	95

certainly not be neglected as compared to the target injection width.

In Fig. 8, photographic images of two so-called 50 μm injections (obtained after displacing the movable wall over the same distance $=100$ μm) taken at the same position in the channel are shown, giving an indication of the current degree of reproducibility of the technique. Again, the peaks are broader than the target value (50 μm) due to the inward diffusion occurring during the injection procedure.

A summary of the experimental $w_{b,inj}$ values obtained for injections with $w_{displ} = 100$ μm and $w_{displ} = 200$ μm is given in Table 2. Experiments carried out for $w_{displ} = 400$ μm and $w_{displ} = 500$ μm (not represented here) showed that the relative difference between the observed peak width $w_{b,inj}$ and the target injection width value ($w_{inj,conv}$, see Eq. (15)) decreased with increasing $w_{inj,conv}$. This is in agreement with the fact that, as the convective contribution becomes larger and larger, it is straight forward to find that the contribution of the diffusion injection width becomes less important.

From the recorded tracer distribution curve, we have also calculated the volume of the injected peaks by calculating the surface under the curves according to Eq. (11) and then multiplying this value (cf. Eq. (12)) by the channel depth d and the channel width

λ_w (arbitrarily set at $\lambda_w = 1$ mm). These values are also represented in Table 2, showing that the injection volumes are of the order of 10 pl, quite similar to the injection volumes in on-chip CE [7].

3.3. Detection groove

Fig. 9 shows the calculated velocity profiles in the detection groove. A recirculation vortex can be noted in both cases. The calculated dispersion curves for the passage of a tracer peak through the rectangular and the semi-circular are presented in Fig. 10 where the peak profiles ($=$ responses at a virtual detection plane) obtained 2 μm after the groove are compared with those 2 μm before the groove. It can clearly be noted that the groove leads to significant band broadening (in a nearly identical manner for the rectangular and the semi-circular groove), but as will be shown below, the resulting loss in theoretical plate numbers is still acceptable. To quantify this argument, the variances σ_t^2 of the different peaks have been calculated by numerical integration. The obtained results are presented in Table 3, showing a small, though significant difference between the rectangular and the semi-rectangular groove. Table 3 also gives the mean detector cell residence time,
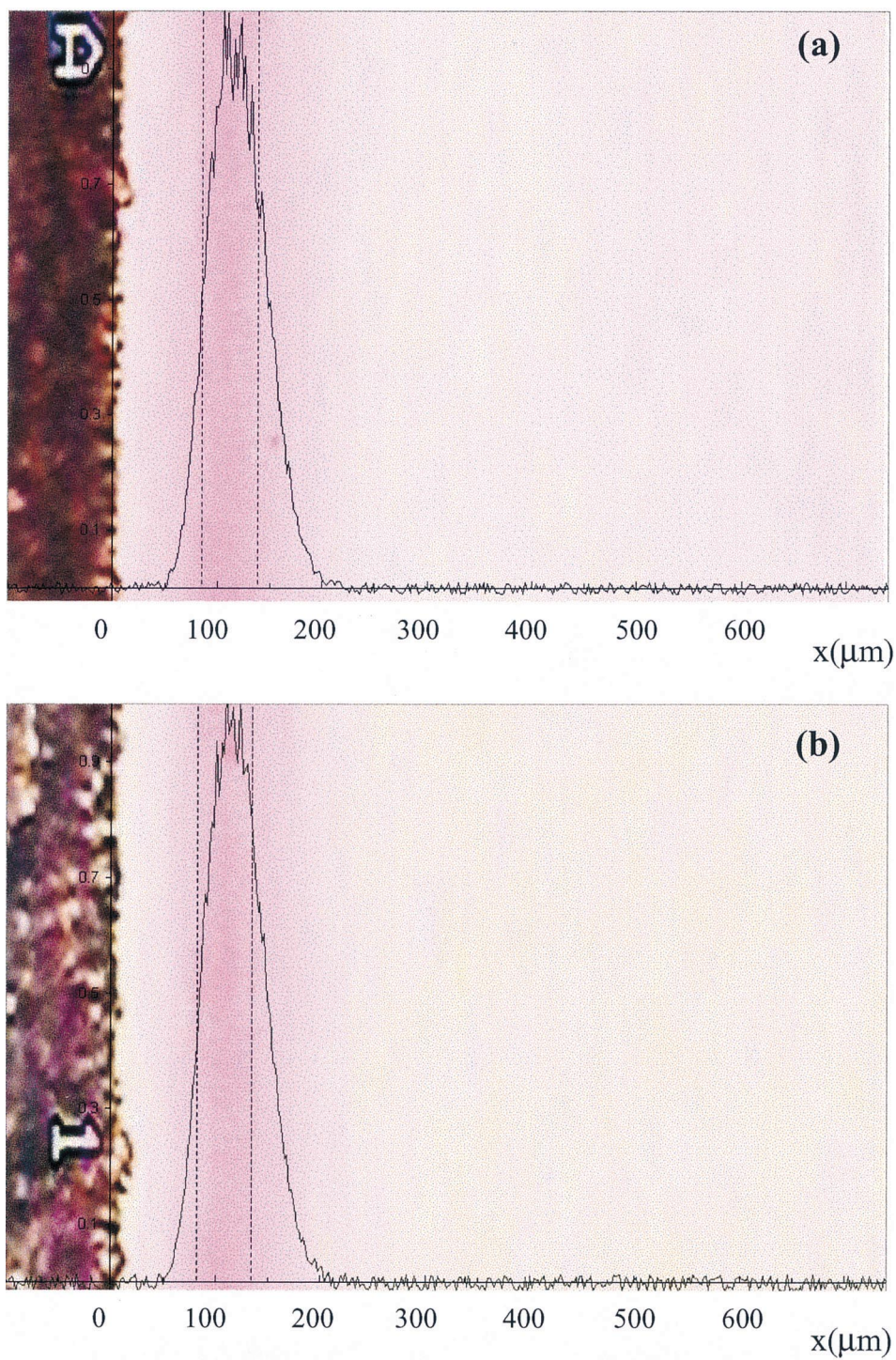
Fig. 8. Still image and colour intensity scan of two different tracer band injections (a and b) obtained by shifting the movable channel plate over a distance $w_{displ} = 100$ μm (displacement velocity $\cong 0.1$ mm/s, channel depth $= 0.1$ μm). Peak volumes were determined to be $V_p = 8.4$ pl for (a) and $V_p = 7.7$ pl for (b).
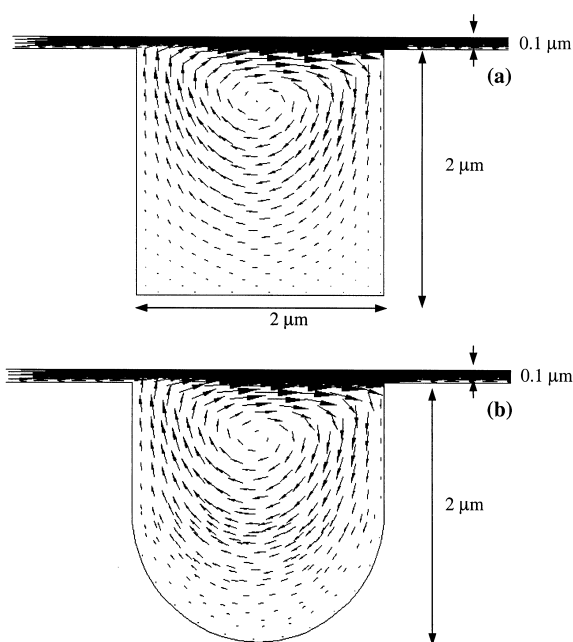
Fig. 9. CFD calculated velocity profiles in rectangular groove (a) and semi-circular groove (b). Velocity of moving wall $u_{wall} = 3.4$ cm/s, mean velocity in in-out outflowing channels $u = 1.7$ cm/s (velocity scale in cm/s).

obtained by numerically determining the first order moments of the peak curves.

4. Discussions

4.1. Injection experiments

Considering that the time needed to establish the linear velocity profile characteristic for a fully developed shear-driven flow is given by $t = 4(\eta d)^{1/2}$ [21], and is hence of the order of 0.04 ms in a 0.1 μm channel ($\eta = 10^{-3}$ kg m^{-1} s^{-1}), the shape of the injected tracer bands can theoretically be expected to be a perfectly rectangular block. Considering that the liquid in a shear-flow driven channel moves at one half of the moving wall velocity (cf. Eq. (1)), the width of the injected block should be given by:

$$w_{inj,conv} = w_{displ}/2 \tag{15}$$

wherein $w_{inj,conv}$ (=target injection width value) represents the expected band width due to the
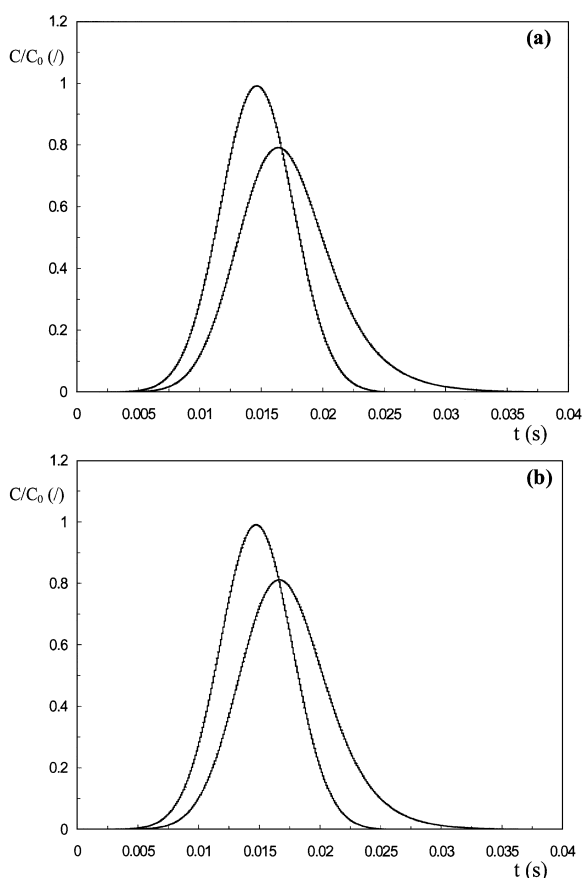

Fig. 10. Simulated broadening of a chromatographic peak with width $w_b = 200$ μm passing through a rectangular (a) and a semi-circular (b) transversal detection groove. The first peak is taken 2 μm before the groove, the second peak is taken 2 μm after the groove (geometry and flow conditions as in Fig. 9).

convective displacement action over a given distance w_{displ}. However, as has already been pointed out by several authors [22,23] investigating the influence of injection band width on the separation efficiency of miniaturised capillary electrophoresis systems, diffusion band broadening occurring during the injection process contributes strongly to the final injection width when it is attempted to inject plugs of the order of 100 μm or smaller [23]. It is therefore not surprising to find that the experimental injection peak widths $w_{b,inj}$ in the third column of Table 2 are consistently broader than predicted by Eq. (15).

To estimate what the injected peak width would have been in the absence of the inward diffusion

Table 3

$\sigma_{x,det}^2$-values obtained from CFD simulations and comparison with the models presented in Fig. 10

	Position	t_m (s)	$\sigma_{t,det}^2$ (10^{-5} s^2)	$\sigma_{x,det}^2$ (10^{-9} m^2)		
				CFD	Model 1	Model 2
Rectangular groove	$x = 498$ μm	0.01459	0.875	2.530		
(u = 1.7 cm/s)	$x = 502$ μm	0.01719	1.696	4.901		
	Difference =	**0.00260**	**0.820**	**2.371**	**1.764**	**2.065**
Semi-circular groove	$x = 498$ μm	0.01459	0.875	2.530		
(u = 1.7 cm/s)	$x = 502$ μm	0.016994	1.514	4.376		
	Difference =	**0.00235**	**0.639**	**1.846**	**1.764**	**2.065**

flux, Eq. (10) can be used to calculate a corrected (i.e., after subtraction of the peak width contribution $\delta_{10\%}$ of the diffusive flux) value $w_{inj,corr}$ for the injection band width:

$$w_{inj,corr} = w_{p,inj} - \delta_{10\%} = w_{p,inj} - \sqrt{5.382 D_m t} \qquad (16)$$

The data presented in the last column of Table 2 are calculated according to Eq. (16), using the experimentally determined D_m value given in Eq. (14) and replacing t by the duration t_{inj} of the injection process which could be estimated from the video recordings. It can be noted that, after correcting for the inward diffusion flux, a fairly good agreement with the target peak width (i.e., the peak width $w_{inj,conv}$ which is purely due to the convective injection process) is obtained. For the $w_{displ} = 100$ μm-experiments ($w_{inj,conv} = 50$ μm), a statistical analysis yields a mean value of $w_{inj,corr} = 64$ μm (± 5 μm). For the $w_{displ} = 200$ μm-experiments, a mean value of $w_{inj,corr} = 102$ μm (± 8 μm) is obtained, which is already very close to the expected target value $w_{inj,conv} = 100$ μm. In both cases, the difference between the uncorrected and corrected values is very large, pointing out the importance of short injection times. In the present study, these were fairly large, because the entire procedure was performed manually. To reduce the undesired contribution of the diffusive flux, the entire injection procedure should be automated, using for example a high resolution automatic displacement systems, and using an piezo-electric nozzle system for the sample and mobile phase liquid dispensing and flushing operations. It should also be reminded that the presently envisioned 50 μm injections are in fact

already at the extreme of what is needed: according to Table 1, a 164 μm wide injection for example already allows to obtain 220 000 plates in a channel which is only 5 cm long.

4.2. Detection experiments

The concept of the detection groove presented in Fig. 4 is related to the bubble-shaped detection cell proposed by Xue and Yeung [3]. The major difference is that in the present case, the axial width of the cell is limited to a few μm. This is a design rule stemming from our CFD calculations, which revealed that, if the axial cell width is larger than 2 μm, a recirculation vortex is generated which causes a detrimental peak broadening (in the CE bubble-cell application, the electro-osmotic flow generated no recirculation vortex). The existence of the recirculation vortices in the shear-driven flow system can be understood from the following basic argumentation: the moving upper wall exerts a viscous force on the entire fluid mass occupying the groove, and would normally create a flow rate of the order $F = u_{wall}/2\delta_G\lambda_w$, whereas only a flow rate $F = u_{wall}/2d\lambda_w$ is allowed to leave the detection groove. To compensate for the excess flow rate, a recirculation vortex (with negative axial velocity) is created, such that the net flow rate in each vertical plane of the system is identical and equal to $F = u_{wall}/2d\lambda_w$.

At first sight, it is difficult to assess whether the presence of the recirculation vortex plays a positive or a negative role in the detector cell band broadening. On the one hand, the negative fluid velocities in the bottom of the groove certainly create an undesired peak broadening effect, whereas on the other

hand the convective effect in the *y*-direction certainly helps speeding up the mass transport between the upper high velocity zone and the bottom stagnant zone. To investigate this more closely, two different models, representing the two extreme cases of mass transport, are considered (see Fig. 11). In the first model, the detection groove is assumed to be a perfectly mixed zone, whereas in the second model the groove is considered to act as a stagnant zone, i.e., as a stationary phase with $K = 1$ and $D_s = D_m$ and exchanging tracer with the mobile phase flow by pure molecular diffusion.

For the first model, the variance in the time ($\sigma^2_{t,\text{det}}$) and the space domain ($\sigma^2_{x,\text{det}}$) can be calculated from the residence time in the detector cell volume:

$$t_{\text{det}} = \frac{V}{F} = \frac{\lambda_G(\delta_G + d)\lambda_w}{ud\lambda_w} \tag{17}$$
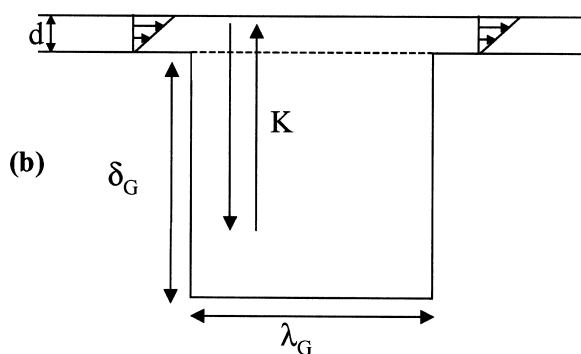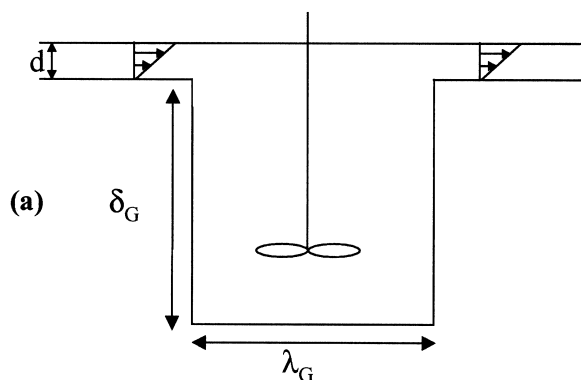
and from:

(a)

(b)

Fig. 11. Perfectly mixed cell (a) and stagnant zone (b) model for the prediction of the detector cell band broadening.

$$\frac{\sigma^2_{t,\text{det}}}{t^2_{\text{det}}} = \frac{1}{N} = 1 \tag{18}$$

yielding:

$$\sigma^2_{t,\text{det}} = t^2_{\text{det}} = \frac{\lambda_G^2(\delta_G + d)^2}{u^2 d^2} \tag{19}$$

And from:

$$\sigma^2_{x,\text{det}} = u^2 \sigma^2_{t,\text{det}} \tag{20}$$

we obtain:

$$\sigma^2_{x,\text{det}} = \frac{\lambda_G^2(\delta_G + d)^2}{d^2} \tag{21}$$

For the second model, $\sigma^2_{x,\text{det}}$ can be calculated by defining a retention factor k_{det} such that it represents the tracer retaining effect (with $K = 1$) of a stagnant layer (thickness δ_G) in contact with a mobile phase layer with thickness d:

$$k_{\text{det}} = \frac{\delta_G}{d} \cdot K = \frac{\delta_G}{d} \tag{22}$$

With Eq. (22), the mean residence time of the tracer peak in the detector cell can be estimated from the conventional chromatographic retention time expression:

$$t_{\text{det}} = \frac{\lambda_G}{u}(1 + k_{\text{det}}) \tag{23}$$

The peak broadening effect of the chromatographic exchange process can then be described by the Van Deemter-expression for SDC, given in Eq. (2), and by putting $k = k_{\text{det}}$, $d_s = \delta_G$ and $D_s = D_m$:

$$H_{\text{det}} = \frac{2}{u}$$
$$\cdot \left[D_m(1 + k_{\text{det}}) + \frac{1 + 7k_{\text{det}} + 16k_{\text{det}}^2}{30(1 + k_{\text{det}})} \cdot \frac{u^2 d^2}{D_m} \right.$$
$$\left. + \frac{k_{\text{det}}}{3(1 + k_{\text{det}})^2} \cdot \frac{u^2 \delta_G^2}{D_m} \right] \tag{24}$$

With Eq. (24), the space domain variance ($\sigma^2_{x,\text{det}}$) predicted by model 2 of Fig. 11 for a detector

positioned the mid-plane of the groove can then be calculated according to:

$$\sigma^2_{x,\text{det}} = H_{\text{det}}\lambda_G/2 \qquad (25)$$

In Table 3, the values predicted by Eqs. (21) and (25) for the currently considered geometry and flow conditions are compared with the value obtained from the CFD simulations. First, it should be noted that both models yield a very similar $\sigma^2_{x,\text{det}}$ value ($1.76\cdot10^{-9}$ m^2 versus $2.06\cdot10^{-9}$ m^2). This points at the fact that the diffusive exchange in the groove (model 2) occurs relatively rapid, and that, even without the presence of the transport enhancing convective recirculation flux, the groove already behaves as a nearly perfectly mixed cell. Secondly, it can be noted that the band broadening value predicted by the CFD simulations is slightly larger ($\sigma^2_{x,\text{det}} = 2.37\ 10^{-9}$ m^2) than the value predicted by the two models. This can be explained from secondary effects due to the interaction of local convective and diffusive phenomena [20], but the details of this discussion are omitted here. Table 3 also shows that the peak variance for the semi-circular groove is slightly smaller than for the rectangular groove-case ($1.84\cdot10^{-9}$ m^2 versus $2.37\cdot10^{-9}$ m^2). This is in agreement with the physical expectations: the semi-circular groove has a smaller volume than the rectangular groove, and has no rectangular corners. It is also in agreement with the fact that the semi-circular groove has a smaller detector cell residence time (2.35 ms versus 2.6 ms). For larger groove depths, model 1 and model 2 no longer yield similar results, and model 2 (which is more likely to approach the reality for the deep groove-case) predicts much larger, and hence unallowable, σ^2_x values

(e.g., model 2 predicts $\sigma^2_x = 3.02 10^{-8}$ m^2 for a 5 μm deep groove, which is already 15 times larger than for the 2 μm deep groove).

Table 4 presents an estimation of the loss in theoretical plates when a detection groove cell as the one proposed in Fig. 4 would be used in the most critical case, i.e., for a SDC channel with thickness $d = 0.1$ μm, and operated at its optimal velocity u_{opt} ($H = H_{\text{min}}$). For this purpose, $N_{\text{eff,det}}/N_{\text{theo}}$ values were calculated according to:

$$\frac{N_{\text{eff,det}}}{N_{\text{theo}}} = \frac{\sigma^2_{\text{col}}}{\sigma^2_{x,\text{det}} + \sigma^2_{\text{col}}} = \frac{H_{\text{min}}L}{\sigma^2_{x,\text{det}} + H_{\text{min}}L} \qquad (26)$$

using the $\sigma^2_{x,\text{det}}$ values obtained from the CFD calculations presented in Table 3 ($\sigma^2_{x,\text{det}} = 2.37\cdot10^{-9}$ m^2 for the rectangular groove and $\sigma^2_{x,\text{det}} = 1.84\cdot10^{-9}$ m^2 for the semi-circular groove).

Table 4 clearly shows that, although the presence of the detection groove causes a significant loss (order 50%) for the ultra-short channel ($L = 1$ cm), a 5 cm long channel still would yield more than 200 000 plates. In this case, the plate loss is only of the order of 20%, a loss which can easily be compensated for (if needed at all) by increasing the channel length from 5 to 6 cm. This sacrifice is obviously small compared to the large advantage of the detection groove (possibility of UV–Vis detection with a path length in the millimeter range). The fact that the plate loss for the semi-circular groove is a few % smaller than for the rectangular groove of course follows directly from the smaller $\sigma^2_{x,\text{det}}$ value for the semi-circular groove (cf. Table 3). The difference is however so small, that it can be concluded that the exact shape of the groove is only of secondary importance. The small difference should in fact be regarded as a justification for the

Table 4
Estimated theoretical plate loss caused by the presence of a transversal detection groove in a 100 nm SDC channel operated at $u = u_{\text{opt}}$ (same column parameters as in Table 1)

L (cm)	H_{min}	N_{theo}	Rectangular groove		Semi-circular groove	
			$N_{\text{eff,det}}$	$N_{\text{eff}}/N_{\text{theo}}$ (%)	$N_{\text{eff,det}}$	$N_{\text{eff}}/N_{\text{theo}}$ (%)
1	0.18	55 902	24 037	43	27 557	49
2	0.18	111 803	67 237	60	73 832	66
3	0.18	167 705	116 309	69	124 886	74
5	0.18	279 508	220 932	79	231 819	83
10	0.18	559 017	493 584	88	506 880	91

use of the rectangular groove, which can be etched much more easily.

5. Conclusions

The fixation technique using the holding piece shown in Fig. 5 offers the attractive possibility to perform shear-driven chromatography directly underneath the lens of a conventional microscope, using the lens to retain the stationary channel part, and using the optical Table to translate and support the movable channel part.

Although the calculated maximally allowable injection volumes to avoid injection peak broadening in sub-μm SDC are in the pl range, the specific architecture and operation mode of shear-driven chromatographic systems enables the application of a very simple zero dead-volume injection concept with which the desired picoliter volumes can easily be handled. Just as for any other miniaturised system, diffusion band broadening contributes significantly to the injected peak volume. By switching from a manual to a fully automated procedure, capable of limiting the total injection time to a few tens of seconds, it should be possible to further reduce the undesired contribution of the diffusive flux to the injection band volume (in the present study still of the order of 40% for 50 μm injections, and of the order of 30% for 100 μm injections). It should furthermore be noted that the presently considered 50 and 100 μm injection band criteria are somewhat too sharp, because, as can be denoted from Table 1, a 150 μm wide injection would still allow to obtain 220 000 plates in a channel with a length of only 5 cm.

When further miniaturising the current chromatographic equipment, computational fluid dynamics simulations will become increasingly important as a tool for the appropriate design of the shape of the injection and detection sections. The present example (flow through transversally oriented detection groove coupled to a sub-μm, high-velocity micro-channel flows) illustrates this point. The dimensions of the proposed detection groove system (offering optical path lengths in the mm range) are just large enough to allow for an undisturbed passage of a light beam, whereas on the other hand they are still sufficiently

small to avoid excessive band broadening, even in the most critical case of a 0.1 mm thin channel operated at $u = u_{opt}$. This is a fortunate coincidence implying that, as supported by the calculations in Table 4, the detection groove is a viable concept opening the road towards high speed sub-μm SDC. The fact that the detection groove acts as a nearly perfect wave guide, i.e., without axial straying of the light, is an advantage which is exclusively linked to the use of sub-μm thin channels. This is one of the rare examples where miniaturisation would have a favourable influence on the detection aspect.

6. Nomenclature

C	Tracer concentration
C_{max}	concentration at peak maximum
d	thickness mobile phase layer (m)
d_f	thickness stationary phase layer, (m)
D_m	molecular diffusion coefficient, (m^2/s)
D_s	molecular diffusivity in stat. phase, (m^2/s)
F	volumetric flow rate, (m^3/s)
H	height of equivalent theoretical plate, (m)
H_{min}	minimal theoretical plate height (m)
I, I_0	intensity of transmitted light
k	retention factor, (-)
L	column length, (m)
M_0	Surface under C/C_0 tracer concentration curve (m), see Eq. (11)
N	theoretical plate number
$N_{eff,inj}$	effective plate number accounting for injection band width, see Eq. (5)
N_{theo}	plate number due to column band broadening only
t	time coordinate (s)
t_{inj}	duration of injection process (s)
t_R	analysis or retention time (s)
u	mean mobile phase velocity, (m/s)
u_{opt}	mobile phase velocity yielding the minimal H value, (m/s)
u_{wall}	velocity of moving wall (m/s)
$w_{b,inj}$	injection peak width at base (m)
$w_{b,inj}$	peak width at detector plane (m)
w_{displ}	moving wall displacement distance during injection (m)

$w_{inj,conv}$	expected band width due to the convective displacement action over a given distance w_{displ} (m), cf. Eq. (15)
$w_{inj, corr}$	band width after correction for diffusive leakage, see Eq. (16)
$w_{p, inj}$	width of injected band
x	axial coordinate (m)
V	detector cell volume, (m^3)
V_p	peak volume (m^3)

Greek symbols

$\delta_{10\%}$	penetration distance of tracer curve at 10% of C_0 (m)
δ_G	detection groove depth (m)
η	dynamic liquid viscosity, (kg/(ms))
λ_G	axial width of detection groove depth, (m)
λ_w	transversal channel width = optical path length (m)
σ_t^2	peak variance in the time domain (s^2)
σ_x^2	peak variance in the space domain (m^2)

Subscripts

col	column
det	detector
inj	injection
m	mobile phase
s	stationary phase

Acknowledgements

References

[1] H. Poppe, Analusis 22 (1994) 22.
[2] H. Poppe, J. Chromatogr. A 778 (1997) 3.
[3] Y. Xue, E.S. Yeung, Anal. Chem. 66 (1994) 3575.
[4] H.J. Crabtree, M.U. Kopp, A. Manz, Anal. Chem. 71 (1999) 2130.
[5] F. Regnier, B. He, S. Lin, J. Busse, Trends Biotechnol. 17 (1999) 101.
[6] M.M. McEnery, J.D. Glennon, J. Alderman, S.C. O'Mathuna, Biomed. Chrom. 14 (2000) 44.
[7] B. He, N. Tait, F. Regnier, Anal. Chem. 70 (1998) 3790.
[8] G. Desmet, G.V. Baron, J. Chromatogr. A 855 (1999) 57.
[9] G. Desmet, N. Vervoort, D. Clicq, G.V. Baron, J. Chromatogr. A (2001), in press
[10] G. Desmet, G.V. Baron, Anal. Chem. 72 (2000) 2160.
[11] Z. Liang, N. Chiem, G. Ocvirk, T. Tang, K. Fluri, D.J. Harrison, Anal. Chem. 68 (1996) 1040.
[12] H. Salimi-Moosavi, Y. Jiang, L. Lester, G. McKinnon, G. Harrison, Electrophoresis 21 (2000) 1291.
[13] G.J.M. Bruin, Electrophoresis 21 (2000) 3931.
[14] J.C. Fister III, S.C. Jacobson, L.M. Davis, J.M. Ramsey, Anal. Chem. 70 (1998) 431.
[15] N.A. Patankar, H.H. Hu, Anal. Chem. 70 (1998) 1870.
[16] S.V. Ermakov, S.C. Jacobson, J.M. Ramsey, Anal. Chem. 70 (1998) 4494.
[17] C.A.J. Fletcher, Computational Techniques For Fluid Dynamics, Vol I, Springer Verlag, Berlin, 1991.
[18] A. Huau, in: Masters Thesis, Vrije Universiteit Brussel, Design and Study of an Injection and Detection System For Shear-driven Chromatography, 2001.
[19] H.S. Carslaw, J.C. Jaeger, Conduction of Heat in Solids, Clarendon Press, Oxford, 1959.
[20] P. Gzil, in: Masters Thesis, Vrije Universiteit Brussel, Computational Fluid Dynamics Study of Shear-driven Flows Through Channels With A Variable Geometry, 2001.
[21] H. Schlichting, in: Boundary-layer Theory, Mc-Graw Hill, London, 1958, p. 83.
[22] S.C. Jacobson, R. Hergenroder, L.B. Koutny, R.J. Warmack, J.M. Ramsey, Anal. Chem. 66 (1994) 1107.
[23] L. Bousse, B. Dubrow, K. Ulfelder, in: J. Harrison, A. van den Berg (Eds.), Proceedings of the μTAS 1998 symposium held in Banff, Canada, Kluwer Academic Publishers, The Netherlands, 1998, p. 271.